

Physically explainable statistical learning of flat bands in stoichiometric materials from the periodic table

Xiuying Zhang ¹, Yi-Ming Zhao ², Zhigang Song,³ and Lei Shen ^{2,*}

¹Department of Physics, National University of Singapore, 2 Science Drive 3, Singapore 117551, Singapore

²Department of Mechanical Engineering, National University of Singapore, 9 Engineering Drive 1, Singapore 117575, Singapore

³John A. Paulson School of Engineering and Applied Sciences, Harvard University, Cambridge, Massachusetts 02138, USA



(Received 18 January 2023; revised 10 May 2023; accepted 5 June 2023; published 22 June 2023)

Flat-band materials (FBMs) serve as a platform for a variety of exotic properties and applications, such as strongly correlated states, topological states, and superconductivity. However, reported FBMs highly rely on materials engineering, such as Moiré lattices. Here, we demonstrate the acceleration of intrinsic FBM discovery using explainable statistical learning within a periodic table representation (PTR). Our model achieves validation accuracies of 0.81–0.97 for X_2YZ full-Heusler alloys across three different databases and 0.84 for ABC₃ perovskites. Our interpretable model and statistical analysis reveal several important valence electron-related features for FBMs, supported by atomic orbital hybridization theory. We further discuss various physical properties and applications strongly associated with flat bands, including topology, thermal conductivity, electron-phonon coupling, and superconductivity. Finally, we predict 25 high-potential, previously unreported flat-band Heusler alloys using the PTR model, validated by first-principles calculations.

DOI: [10.1103/PhysRevMaterials.7.064804](https://doi.org/10.1103/PhysRevMaterials.7.064804)

I. INTRODUCTION

An electron in crystals feels both single-particle and electron-electron interactions. The single-particle interaction characterized by the bands makes the crystal a normal metal or semiconductor. While the electron-electron interaction predominates over the single-particle interaction, the material will show various exotic quantum phenomena, such as superconductivity [1,2], the fractional quantum Hall effect [3,4], and excitonic Bose-Einstein condensation [5]. Such a situation usually occurs when the material has flat enough bands, i.e., weak dispersion of spectral bands in the momentum space, suppressing the single-particle interaction. One of the most typical flat-band systems might be the twisted bilayer graphene with a Moiré lattice [3,6–9]. The search for new flat-band materials within other two-dimensional (2D) patterned systems, such as Kagome [4,10–12] and Lieb [13–16] lattices, is ongoing and has shown a great success. Besides 2D systems, the flat bands also can exist in three-dimensional (3D) systems such as pyrochlore lattice [17–20]. Recently, Bernevig and his collaborators developed a catalog for 2379 3D flat-band materials in total by analytic methods and high-throughput calculations, in which 35 full-Heusler alloys (FHAs) are reported as the best flat-band candidates, having perfectly flat bands at or very close to the Fermi level (E_f) [21,22].

Despite the recent success in discovering and designing flat-band materials by the experiment and calculation, the exploration of them is slow and expensive. An emerging technique of machine learning (ML) has attracted immense attention in the field of materials science, which can provide

an alternative approach to discover crystals with unique properties quickly and cheaply, such as battery electrode materials with large voltages [23], topological materials with Weyl points [24], high-temperature superconductors [25], and 2D magnetic materials with high Curie temperature [26]. Thanks to the experimental and computational development of materials databases, such as ICSD [27,28], AFLOW [29–33], Materials Project (MP) [34,35], and 2DMatPedia [36,37], the developed materials-related ML models become accurate and reliable. Particularly, ML models show the superior performance for a large family of stoichiometric materials with a type of chemical formulas and structures, such as ABO₃ perovskites, X_2YZ FHAs, $M_{n+1}AX_n$ ($n = 1–3$) MXenes, and C₃A₂D₃O₁₂ garnets. The abundance of crystals with fixed formulas/structures can provide the basis for training ML models without structural features, such as using the periodic table, making the model easier to train [38–41]. Several element-only-based deep learning (DL) models have been successfully developed for the materials science community such as an artificial neural network (ANN) [42], Compositionally Restricted Attention-Based network (CrabNet) [43], and ElemNet [44]. However, none of models have been developed for efficiently predicting flat bands and providing physical explanation to the flat-band properties in stoichiometric materials.

In this work, we develop an explainable deep-learning classification model by combining the convolutional neural network (CNN) with the periodic table representation (PTR) [38], and demonstrate that such DL model cannot only accurately predict flat bands in 3D stoichiometric crystals, but provide explainable physical parameters with statistical analysis. By training more than 50 000 X_2YZ FHA data sets in AFLOW, the accuracy of our PTR model is as high as 0.81 for the validation set from the Materials Project. Besides,

*shenlei@nus.edu.sg

TABLE I. Statistics of total, spin polarized (SP), and non-SP full-Heusler crystals in the AFLOW, Materials Project, and catalog of flat-band stoichiometric materials database, hosting flat bands around the Fermi level under different screening criteria. ΔE and ω is the energy window around E_f and energy dispersion of bands, respectively.

	Spin state	Dataset 1 (AFLOW ^a)	Dataset 2 (Materials Project ^b)	Dataset 3 (Catalog of flat-band stoichiometric materials ^c)
Total number	Non-SP	36698 (70.1%)	893 (74.4%)	35
	SP	15681 (29.9%)	307 (25.6%)	—
At least one high-symmetry path $\Delta E < 1.5$ eV, $\omega < 50$ meV	Non-SP	15506 (29.6%)	368 (30.7%)	—
	SP	14217 (27.1%)	240 (20.0%)	—
At least one high-symmetry path $\Delta E < 0.5$ eV, $\omega < 10$ meV	Non-SP	354 (0.7%)	19 (1.6%)	35
	SP	443 (0.8%)	28 (2.3%)	—
Whole Brillion zone $\Delta E < 1.5$ eV, $\omega < 50$ meV	Non-SP	72 (0.1%)	0	—
	SP	118 (0.2%)	0	—

^aTraining and test data set [30–33].

^bValidation data set 1 [34,35].

^cValidation data set 2 [21].

our model can identify 34 over 35 best full-Heusler flat-band candidates reported by high-fidelity density-functional theory (DFT) calculations [21]. The PTR model is universal and performs well for other crystals, like ABC_3 perovskites, keeping a high validation accuracy of 0.84. It demonstrates the robustness and generalization of our PTR model. To uncover the CNN “black box”, we visualize the hidden layers of the PTR model with the principal composition analysis (PCA) and compare with statistical analysis on FHAs. It is found that the first-principals component (PCA1) has a direct relationship with the mean number of the valence electrons (MNV) with a period of $3n$ (n is integers), which is due to the additional $3n$ electrons from elements with fully occupied d and/or f orbital. Such a periodic trend indicates that the number of valence electrons is an important physical descriptor for the flat-band prediction, which is further confirmed by our statistical analysis on the data set. Furthermore, we find that the flat rate is as high as 0.91 for the spin polarized (SP) FHAs, which can be physically explained by the Slater-Pauling rule [45,46] and the band spin splitting. Interestingly, for the non-SP compounds, two flat rate peaks around 16 and 24 of the total number valence electrons (TNV) are found. Two such magic numbers of the flat rate are explained by the orbital hybridization theory. The combination of the statistical learning, data analysis, and orbital hybridization model in this work not only gives a detailed physical explanation for the formation of flat bands, but also provides a quick and economical way for discovering and designing flat bands in other stoichiometric crystals, for example, ABC_3 perovskites. Finally, 19 high-potential, new full-Heusler alloys and six previously unreported half-Heusler alloys with flat bands very close to the Fermi level are predicted by the PTR model (Supplemental Material [47]).

II. METHODS

Screening data. The training data set of FHAs are from the AFLOW database through the RESTful API [31–33]. We get a total of 61 692 full-Heusler crystal structures and band

structures which are calculated by the high-throughput DFT framework. The spin-orbital interaction is neglected as it does not drastically affect the band structure around the Fermi energy. Considering the practical applications, the crystals with rare earth (Sc, Y, Lanthanides) and the radioactive elements are removed from the data set. Finally, there are a total of 52 379 full-Heusler crystals for training the model.

Flat bands are defined along at least one full high-symmetry path in the Brillion zone as these flat bands are symmetry protected and physically meaningful. The energy window ($\Delta E = |E - E_f|$) of the flat bands is set as 1.5 eV because the electronic property of a crystal is mainly defined by the electrons around the E_f . Finally, the energy dispersion (ω) is bound within a narrow window of 50 meV. A wider or narrower flat-band threshold would filter out more or fewer crystals with flat bands [12] as shown in Table I. Full-Heusler crystals with several special flat-band thresholds can be found in the Supplemental Material (Tables S3–S5) [47]. According to our definition, about half of the crystals (29 723/52 379) in our database have a flat band close to the E_f . Such a balanced data set is helpful for training the model to get a more reliable classification result.

We adopt two data sets of FHAs from other databases for validation. One is from the Materials Project [34,35], in which there are around 2000 FHAs. The other one is from “Category of flat-band stoichiometric materials” [21], in which 35 FHAs are claimed as the best flat-band candidates by DFT calculations.

PTR model. Since our database are all full-Heusler crystals, only elemental properties are needed for distinguishing a crystal for a machine. The atomic properties are closely related to the position of the element in the periodic table. Therefore, the atomic properties could be directly extracted from the periodic table, and in consequence, the periodic table is a natural descriptor of a crystal. With this understanding, we use a specific type of deep learning network, named the periodic table representation (PTR) classification model. It is a supervised CNN model and just uses the periodic table figure as the input without any manually picked features and thus

greatly minimizes human involvement. Every full-Heusler crystal is transformed into a two-dimensional periodic table figure with five rows and 17 columns, and then the figure is denoted by a matrix A . The corresponding site in matrix A is initialized by -0.1 if the site is taken by the 55 elements that our data sets contain, and initialized by 0 if the element is not contained. The periodic table should capture the difference between elements occupying the X site and those occupying Y or Z site (YZ sites). It is because the full-Heusler crystals have the chemical formula of X_2YZ and elements at the X site have a different chemical environment to those at the YZ sites. The X site atoms form a simple cubic crystal with an octahedral (O_h) symmetry, while the atoms located at YZ sites form a body-centered-crystal with a tetrahedral (T_d) symmetry. Then, the value of the corresponding X site element in the periodic table is set to 2.6 in matrix A , and those YZ site elements are set to 1.3 to keep the mean of matrix A is always equal to zero. With such a method, the normalization process is no longer needed. The periodic table is used as the only input feature for our *ab initio* deep learning model without any other manual featurization. In another example of ABC_3 perovskites, except the element A , B , and C , all the remaining elements are firstly set as -0.1 in the periodic table matrix. To guarantee the mean value of the whole matrix to be zero, the A and B sites are set as 1.1, and C as 3.3 because the number of the C atoms is three times of the A and B atom in a perovskite unit cell. Then, the PTR model is ready to be trained for the flat-band prediction of perovskite crystals.

The input figure is then transferred into the PTR model which includes three convolutional layers that are used as the feature extractor, and two full connection layers that are used for data prediction. The crystals with flat bands along high-symmetry path are labeled as 1, and those without flat bands labeled as 0. To be more specific, 96 convolutional maps are used in each convolutional layer which is followed with a rectified linear unit (ReLU) layer. The ReLU has a nonlinear activation function $f(x) = \max(0, x)$. In the training process, the negative log likelihood loss (NLLLoss) function is used to quantify the model. The model is fully trained after the accuracy is converged with the optimization method of stochastic gradient descent (SGD), a starting learning rate of 0.01 and a momentum of 0.9. The convolutional filters are set as 3×3 , 5×5 , and 3×3 for the three convolutional layers, respectively, and the stride is set to be 1. Also, a zero padding of one is used for the first two convolutional layers by adding zeros around the border to preserve as much information as possible in the early layers. The input volumes are 19×7 , 19×7 , and 15×3 , for the three convolutional layers, respectively, and the generated convolutional maps after the convolution are 17×5 , 15×3 , and 13×1 , respectively. The code is available in Ref. [65].

Number of valence electrons. For counting MNV, we include the fully occupied d orbital and f orbitals, which could differentiate the elements in the same group in the periodic table. For example, 28 valence electrons ($[Xe]4f^{14}5d^{10}6s^26p^2$) are considered for the Pb atom. For counting TNV, we do not consider the fully occupied d orbital and f orbitals. Thus, the Pb have four total valence electrons ($6s^26p^2$). We only take the non-spin-polarized crystals into

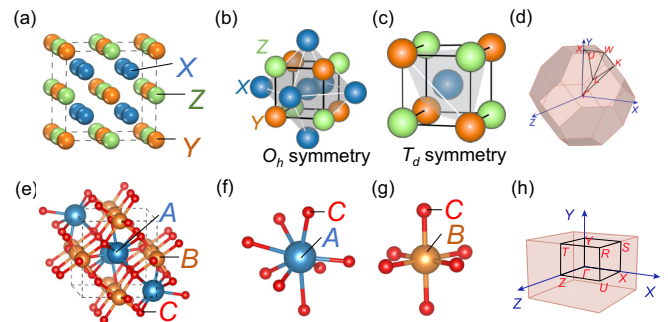


FIG. 1. Crystal structures of two typical categories of stoichiometric materials, X_2YZ full-Heusler alloys and ABC_3 perovskites. (a) Crystal structure of a cubic $L2_1$ full-Heusler conventional cell (space group $Fm\bar{3}m$, No. 225). (b) X site (blue) atoms locate at the Wyckoff position $8c$ ($\frac{1}{4}, \frac{1}{4}, \frac{1}{4}$), forming an O_h site symmetry and a simple-cubic sublattice. (c) Y (orange) or Z (green) site atoms locate at the Wyckoff position $4a$ ($0, 0, 0$) and $4b$ ($\frac{1}{2}, \frac{1}{2}, \frac{1}{2}$), respectively, forming a T_d site symmetry and a face-centered-cubic sublattice. (d) Irreducible Brillouin zone of conventional fcc lattice. Path: Γ ($0, 0, 0$), X ($1/2, 0, 1/2$), W ($1/2, 1/4, 3/4$), K ($3/8, 3/8, 3/4$), L ($1/2, 1/2, 1/2$), U ($5/8, 1/4, 5/8$). (e) Crystal structure of an orthorhombic ABC_3 perovskite conventional cell (space group $Pnma$, No. 62). (f) A site atoms occupy the $4c$ (cuboctahedron) position and (g) B site atoms are on the $4d$ (octahedron) position. (h) Irreducible Brillouin zone of ABC_3 perovskites. Path: Γ ($0, 0, 0$), X ($1/2, 0, 0$), S ($1/2, 1/2, 0$), Y ($0, 1/2, 0$), Z ($0, 0, 1/2$), U ($1/2, 0, 1/2$), R ($1/2, 1/2, 1/2$), T ($0, 1/2, 1/2$).

consideration for TNV flat-band analysis as more than 90% of the spin polarized FHAs have flat bands.

DFT calculations. The band structures and density of states of the full-Heusler crystals in this work are all calculated with the DFT method based on the first-principles theory in the VASP code [48,49]. The projector augmented wave method [50] with the cutoff energy of 600 eV is employed. The exchange-correlation functional is evaluated within the generalized gradient approximation function [51] in the scheme of the Perdew-Burke-Ernzerhof parameter. The geometric crystal structure is firstly fully optimized with the force convergence threshold of 0.01 eV/\AA . The self-consistent calculations are converged with a reciprocal space Monkhorst-Pack grid [52] sampling of size $15 \times 15 \times 15$ in the irreducible Brillouin zone (BZ) for a unit cell and energy threshold of 10^{-6} eV .

III. MODEL PERFORMANCE

The $L2_1$ full-Heusler compound has a face-centered cubic (fcc) crystal structure with space group of $Fm\bar{3}m$, No. 225, and a stoichiometric composition X_2YZ . The primitive cell of a full-Heusler contains two atoms sitting at the Wyckoff position $8c$ ($1/4, 1/4, 1/4$) (X site), one atom at $4a$ ($0, 0, 0$) (Y site), and one atom at $4b$ ($1/2, 1/2, 1/2$) (Z site) [Fig. 1(a)]. Atoms at the X site have the O_h symmetry [Fig. 1(b)] and those at the Y or Z site have the T_d symmetry [Fig. 1(c)]. The perovskite structure of ABC_3 has a much lower symmetry compared with Heusler alloys, which is orthorhombic with space group of $Pnma$, No. 62 [Figs. 1(e)–1(h)]. In the final part of this work,

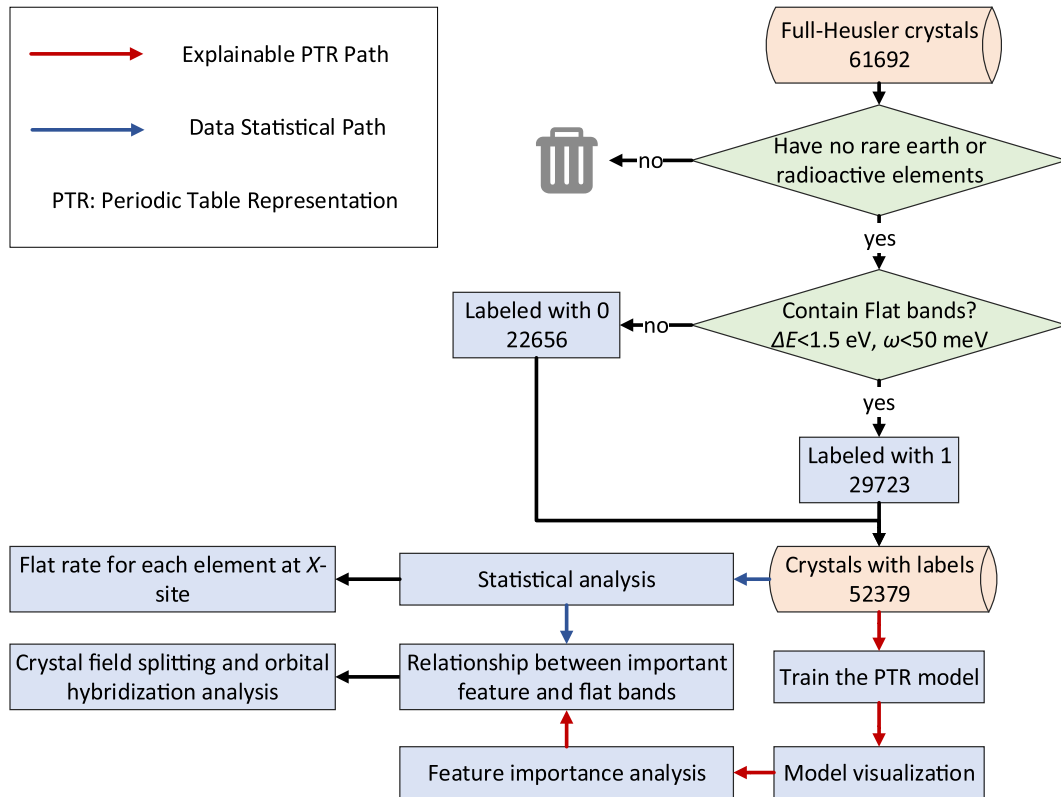


FIG. 2. Work flowchart of this study. The full-Heusler crystals are obtained from AFLOW database. The flat bands are defined with the threshold of $\Delta E < 1.5$ eV and $\omega < 50$ meV and 29723 flat-band and 22656 non-flat-band full-Heusler crystals are labeled, which are used for statistical analysis and training the PTR model. The explainable PTR model is then used to extract physical features from the hidden layers of the neural network. Finally, statistical analysis and a physical mechanism is applied to help explain the model. The red arrows show the explainable deep-learning path, while the blue arrows indicate the data statistical path.

using perovskites as example, we demonstrate that our model is not only applicable for crystals with the large data set and high symmetry, but also applicable to the small data set and low symmetry. We take 61 692 FHAs and corresponding band structures in AFLOW for both the statistical analysis and ML model development of flat bands in this work. Before training the ML model, the outliers and unsuitable compounds in the data set are cleaned (Fig. 2) as declared in the method part. Finally, 52 379 full-Heusler crystals are used for study, which is randomly divided into training, validation, and test sets in the ratio of 0.8:0.1:0.1. The training, validation, and test set are used for training the model, tuning the hyperparameters, and providing a fair evaluation of performance metrics across other ML models, respectively. To define the band flatness from band structures, the flat band segments along the high-symmetry path in the BZ [Fig. 1(d)] around the Fermi level are taken into consideration. The parameter of the energy window (ΔE) is to confirm that the flat bands locate around E_f , which is meaningful for practical applications in devices. The other parameter of the energy dispersion (ω) is to identify “flat” bands along the path between high-symmetry points within the energy window (see details in the Methods section). Under the threshold of $\Delta E < 1.5$ eV, and $\omega < 50$ meV, about half of FHAs have flat bands (Table I). A more strict or loose threshold will clearly filter out more or fewer alloys with flat bands. Even under a very strict threshold of $\Delta E < 0.5$ eV, and $\omega < 10$ meV, 797 (AFLOW) and 47 (MP) alloys still satisfy

the criteria. Interestingly, there are 190 alloys (AFLOW) have flat bands along the whole BZ (see details in Fig. S7 and Table S4). Considering a tradeoff between the size of data sets and the quality of flat bands, the threshold of $\Delta E < 1.5$ eV and $\omega < 50$ meV are used in the remaining part unless otherwise stated.

After data collection and classification, we transform each alloy into the corresponding 2D periodic table fragment matrix for the PTR model classification [see examples of Cu_2MnAl and Fe_2HfSn in Fig. 3(a), and more details in the Methods section]. Our PTR model achieves the accuracy of 0.86 and 0.83 on the validation and test sets, respectively. Specifically, this means that the PTR algorithm can predict the flat band around E_f for full-Heusler compounds with an accuracy larger than 80% only using the information of the chemical formula. It is found that when the X site is occupied by the Co, Mg, Ge, Cd, Sn, and Hg, the average accuracy is greatly increased to 0.92 [Fig. S1(a)]. The accuracy at YZ site is much high and uniform for all elements [Fig. S1(b)]. Thus, the flat bands in FHAs are mainly affected by the X site elements.

IV. MODEL VALIDATION

To estimate our PTR model’s generalized and robust capability, we directly apply it on ~ 1200 FHAs in MP database as the validation data set. All of them are not seen by the model

(a) Periodic Table Representation model

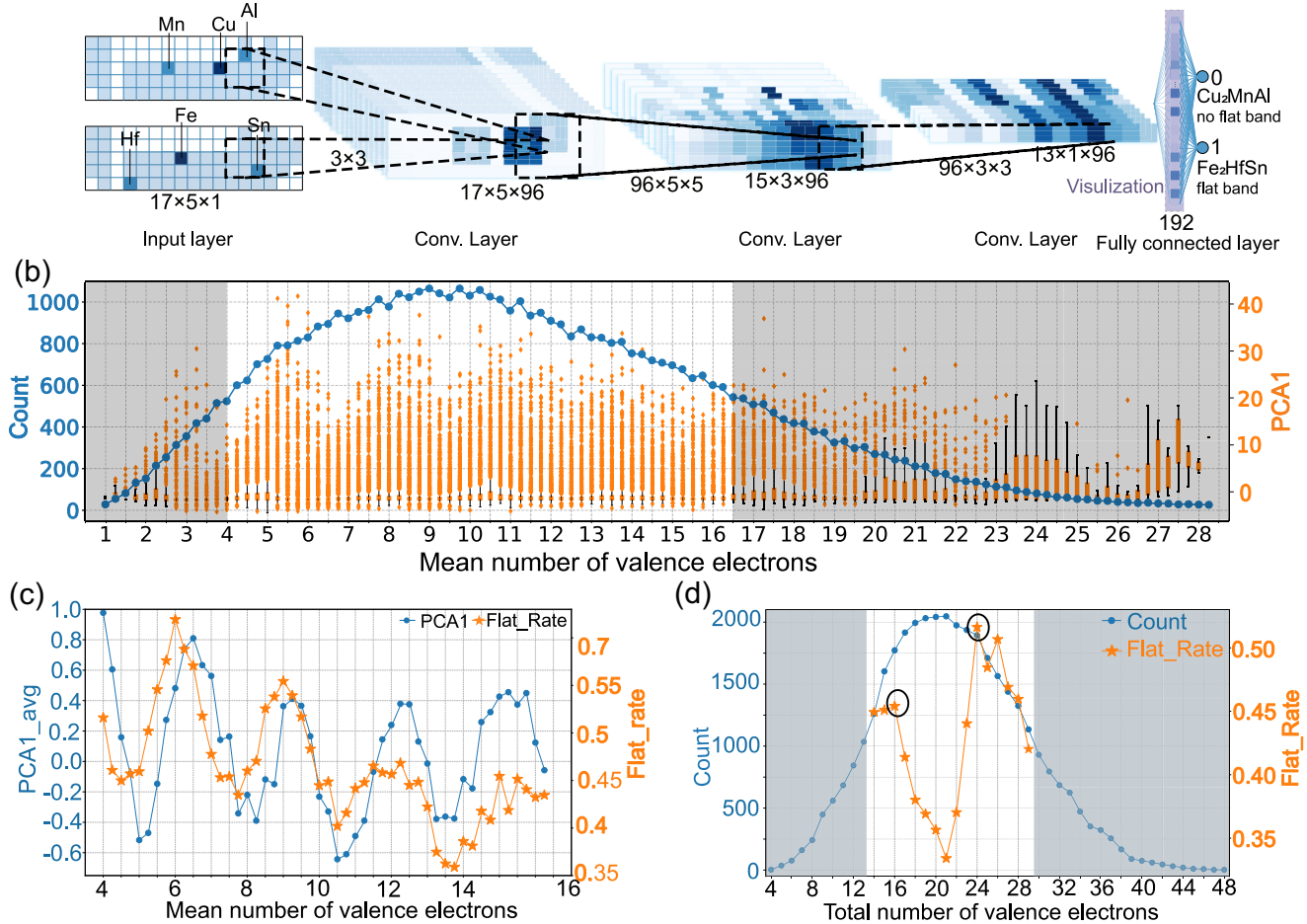


FIG. 3. (a) Structure of the periodic table classification model. The input images take the non-flat-band Cu_2MnAl and flat-band Fe_2HfSn as examples. The output of Cu_2MnAl and Fe_2HfSn is classified as 0 and 1, respectively. The color code in the periodic table: Cu/Fe (X site) is dark blue, Mn/Hf and Al/Sn (YZ sites) are blue, the other elements are light blue, and the elements not in any full-Heusler alloys are white (see elemental details in Fig. S1 [47]). The last hidden layer (purple shaded layer) is picked out for the model visualization. (b) The count of full-Heusler alloys (blue solid circles) for *mean* valence electrons and the PCA1 value for each compound (orange solid diamonds). The FWHM of the count distribution is used for our analysis and highlighted within a white area. (c) PCA1 averaged (blue solid circles) over the MNV of full-Heusler unit cells and flat rate (orange solid stars) of the corresponding MNV. (d) Flat rate (orange solid stars) and the count of alloys (blue solid circles) for *total* valence electrons of a unit cell of non-SP full-Heusler crystals. Two flat-rate peaks within FWHM are highlighted by two black circles.

during the training process. It is found that the PTR model can also get an accuracy of 0.81 for the MP data set. Moreover, using the best flat-band candidates of 35 FHAs reported in a previous work [21] as another validation, our PTR model can identify 34 of them except Ru_2FeSi . It is worth noting that the paramagnetic state of Ru_2FeSi is used in Ref. [20]. However, Ru_2FeSi is a ferromagnetic alloy [34]. The flat bands are destroyed by the spin-polarization effect (Fig. S2 [47]). Such results reconfirm that our PTR model can correctly predict flat bands near E_f for either spin polarized or non-SP FHAs.

Model visualization and explanation. Our PTR model shows its strong capability to automatically predict flat bands with a high accuracy, but does the PTR model predict the flat bands based on the logical descriptors? To answer this question, it is necessary to unravel the neural network internal operations. To open the black box and understand the physics behind our PTR model, we resort to visualization

process with the principal composition analysis [23] through pulling out data in the last two fully connected layers. Our PTR model identifies that the number of valence electrons, including mean and total, as the most important features for the flat-band prediction. The PCA1 results show a periodic oscillation of the *mean* number of valence electrons (MNV) per atom [Fig. 3(b)]. Note that we only use the full width at half maximum (FWHM) of the count distribution for our next analysis, corresponding to the MNV in the range of 4 to 16.5 [Fig. 3(b)], because the statistical analysis is meaningless for small number of crystals. Figure 3(c) shows a clear periodic relationship between PCA1 and the MNV, i.e., a period of 3. It means that the MNV must be a crucial parameter for flat bands in FHAs because the first-principles composition analysis is the most important component in the PTR model. To further verify whether the mean number of valence electrons learned from PCA1 is the predominant parameter

for flat bands, we calculate the flat rate for each MNV, which is the ratio between the number of the crystals having flat bands and the total number of crystals. Obviously, the flat rate has the relationship with the MNV or the same trend to PCA1 [Fig. 3(c)]. In summary, our PTR model has learned the underlying physics of flat-band information automatically, which is supported by the statistical analysis.

The periodic behavior of MNV with the flat-band rate in Fig. 3(c) originates from accounting of electrons in fully occupied d or f orbitals as introduced in the Methods section. For example, Ge has 14 valence electrons ($[\text{Ar}]3d^{10} 4s^2 4p^2$) according to the magpie features. In the same group VIA, Ge possesses the same number of valence electrons as C and Si [four valence electrons ($s^2 p^2$)] if the fully occupied d orbital is ignored, and exhibits similar electronic behavior. Thus, on average, about 12 more electrons (10 for d and 14 for f), corresponding to three electrons per atom (a full-Heusler alloy consists of four atoms), are accounted for when calculating the number of valence electrons for elements in a full-Heusler alloy. If two such elements are present, six more valence electrons are counted per atom, and so on. If the fully occupied d or f orbitals are excluded from valence electron counting, the periodic behavior of the flat-band rate with the MNV disappears [Fig. 3(d)], validating our explanation for the periodic behavior in Fig. 3(c).

The relationship between valence electrons and flat bands discovered by our explainable PTR model should be physically reasonable. It is because many other physical properties of full-Heusler compounds are decided by the valence electron count (N_V) [46,53–56]. For example, the magnetic moment per unit cell (m) of FHAs can be roughly predicted through the Slater-Pauling rule ($m = N_V - 24$) [46]; the Curie temperature is linearly dependent on N_V ; most full-Heusler compounds with 24 valence electrons are semiconductors [53]; nonmagnetic full-Heusler crystals with N_V of around 27 usually have a high superconducting transition temperature [55,56]. Furthermore, the main difference in electronic structures of FHAs is the location of the E_f , which is mainly determined by the N_V . Therefore, the existence of flat bands around the E_f should have a strong correlation with the number of valence electrons, which can be further validated by the statistical analysis on the data set.

Statistical analysis. To statistically study the elemental contribution to the flat band, we separate the X site from the YZ sites. It is because Fig. S3 [47] shows that the flat rate is relatively large if the X site is occupied by $3d$ -transition-metal (TM) elements or s elements. We then revisit all full-Heusler band structures with $3d$ -TM elements occupying the X site. It is found that almost all of them have at least one flat band along the high symmetry paths, although some flat bands are far from E_f or crossed by other bands. Further physical inspections found that the flat band is only contributed by the e_u^* orbital (contributed by d_{z^2} and $d_{x^2-y^2}$) of the X site $3d$ -TM elements [see an example in Figs. 4(a)–4(b)].

Further data analysis (Table I) indicates that SP materials have larger flat rate than the non-SP compounds with the values as high as 91% and 78% for AFLOW and MP, respectively. However, the flat rate is only 42% and 41% for the non-SP compounds in these two databases, respectively.

We believe the Slater-Pauling rule, the magnetic moment (M_t) of a full-Heusler crystal obeys $M_t = Z_t - 24$ where Z_t is the total number of the valence electrons [45,57], may be the main reason for the large flat rate of the SP crystal. It is because the spin down bands always contain exactly 12 electrons, which makes the E_f located just below the e_u^* orbital that usually has several flat bands. This behavior makes the spin down band always have flat bands around the E_f and will certainly greatly enhance the flat rate for the SP FHAs. Furthermore, the spin polarization results in a splitting of two subsets of bands (spin-up and spin-down), thus a probability for shifting the flat band (out of ΔE initially) into ΔE .

Next, we take Ca_2ClP , a typical 16 valence-electron full-Heusler alloy, as an example to explain the flat-rate magic number of 16 using the orbital hybridization analysis. Figure 4(e) shows its band structure with a flat band along the Γ -X high symmetry path. The P and Cl atoms form a simple cubic structure, and their p orbitals first hybridize with each other. An antibond (t_{1u}^*) and a bond (t_{1u}) are formed. The s orbitals of the P, Cl, and the two Ca atoms also hybridize, resulting in two of the s orbitals located at the low energy level and the other two located at the high energy level. Then, the 16 valence electrons of Ca_2ClP will fill up eight orbitals, two nondegenerate a_{1u} and a_{1g} and threefold degenerate t_{1u} and threefold degenerate t_{1u}^* bonds [Fig. 4(f)]. After filling 16 electrons, the threefold degenerate t_{1u}^* is just located below the E_f [Fig. 4(f)]. Thus, the flat band along the Γ -X direction is induced by the nonbond threefold degenerate t_{1u}^* . For 15 or 14 valence-electron FHAs, one or two orbitals of t_{1u}^* will be shifting above the E_f , but still leaving two or one nonbond orbital below the E_f . Thus, FHAs with 15 or 14 valence electrons also have a high flat rate compared with those with 16 electrons due to the threefold degenerate feature of t_{1u}^* as shown in Fig. 3(d).

V. DISCUSSION

Generalization of PTR model. So far, we have demonstrated the superior performance of our explainable PTR model for predicting the flat-band behavior in FHAs. Actually, our periodic table-based model is general, and is able to adapt properly to other stoichiometric compounds, like the widely studied ABC_3 perovskites and $\text{A}_3\text{B}_2\text{C}_3\text{D}_{12}$ garnets. For applying the PTR model to such material families, just only the weight of each element in the periodic table graph is needed to be fine tuned according to the element weight in the formula (see details in the Methods section). Using 189 ABC_3 perovskites (SG No.: 62) from the Materials Project, we demonstrate that the accuracy of the PTR model is still as high as 0.84. Thus, the PTR model is applicable for materials with both high and low symmetry. To further demonstrate the universality and applicability of our model, we perform the PTR model to predict new flat-band *half*-Heusler alloys. Besides the new 19 flat-band *full*-Heusler alloys, six high-potential, previously unreported *half*-Heusler alloys with flat bands very close to the Fermi level (-0.5 – 0.5 eV) and a high density of states are discovered and reported in this work (Fig. S9 [47]).

Topology of flat bands. The topological property of flat bands has attracted great interest for quantum devices [3,58,59]. One can use our PTR model to predict flat bands

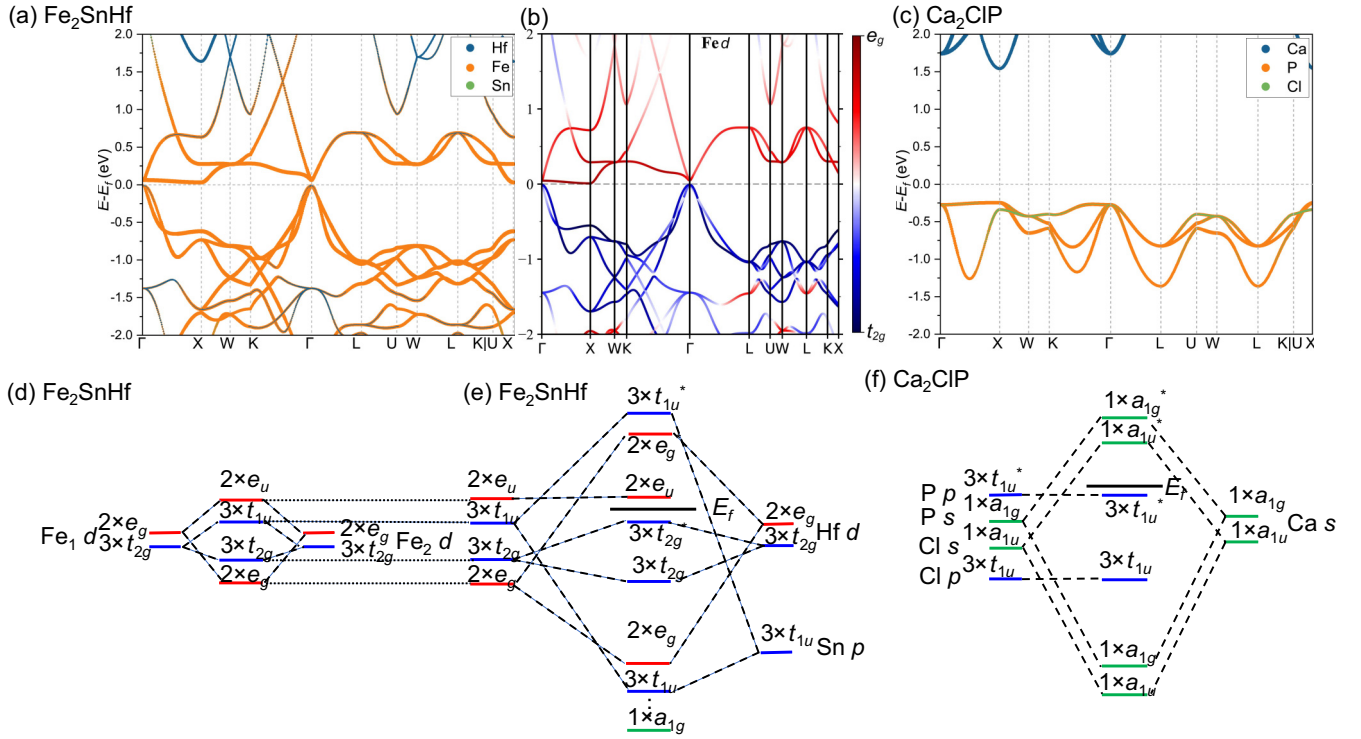


FIG. 4. (a) Element and (b) Fe orbital projected band structures of *spd*-type Fe_2SnHf . (c) Element projected band structures of *sp*-type Ca_2CIP . The color and the line width of the band structure are proportional to the weight of the corresponding elements. The Fermi energy is set to zero. (d) Atomic-orbital energy diagrams of *d* orbitals between two Fe atoms at different sublattices in the unit cell of Fe_2SnHf . (e) hybridizations among Fe_d , Mn_d , and Si_p under the T_d site symmetry of Fe_2SnHf . (f) Atomic-orbital hybridizations among *p* and *s* orbital of P and Cl atom, and *s* orbital of two Ca atoms at different sublattices in the unit cell of Ca_2CIP . Note the orbital symmetry characters are represented under the O_h site symmetry throughout the diagram: representations of *d*-*e* (d_{z^2} , $d_{x^2-y^2}$), *d*-*t₂* (d_{xz} , d_{yz} , d_{xy}), *p*-*t₂* (p_x , p_y , p_z), and *s*-*a₁* states in T_d site symmetry can be transformed into those of e_g , t_{2g} , t_{1u} , and a_{1g} states in O_h site symmetry, respectively.

first. Then, the topological property of the flat band can be further analyzed by DFT calculations. For example, the band structure of Fe_2HfSn with spin orbital coupling (SOC) is shown in Fig. S4(a) [47]. The twofold degenerate conduction bands have several flat bands. The flat band along the X-W, W-K, U-W, and U-X high symmetry paths may be nontrivial because of a gap opening in the presence of SOC [12], while the Γ -X flat band might be topologically trivial.

Seebeck coefficient and electron-phonon coupling. The high density of states on or very close to the Fermi level will induce strong electron-phonon coupling, which is an indispensable factor for the thermal conductor and superconductor. Taking semiconducting Fe_2HfSn and metallic Ni_2NbAl , two stable flat-band FHAs as an example, which have the negative formation energy, small energy above Hull (< 0.01 eV/atom) and no imaginary frequency in the phonon structure [Fig. S5(a) and S5(c)], we calculate the Seebeck coefficient, power factor, and electron-phonon coupling effect. The narrow-bandgap Fe_2HfSn has very large Seebeck coefficients of 600 and $400 \mu\text{VK}^{-1}$ for *n*- and *p*-type doped compound [Fig. S5(b)] because its band asymmetry (asymmetric conduction and valence bands [60,61] as well as the asymmetric conduction band along Γ -X and X-W) [62,63]. The calculated electron-phonon coupling constant and T_c of the superconducting state of Ni_2NbAl is 0.59 and 2.66 K [Fig. S5(d)], respectively, in good agreement with the experiments (2.15 K) [64].

VI. CONCLUSION

A periodic table representation model is developed in this work, which can correctly identify flat band around the E_f in stoichiometric materials. For example, using the Heusler data sets from the Materials Project [34,35] and the catalog of flat-band stoichiometric materials [21] as validation, the model accuracy is 0.81 and 0.97, respectively. The model self-learns the number of valence electrons (mean and total) as two important features for the flat-band prediction, which is confirmed by the statistical analysis. The magic numbers of the large flat rate in non-spin-polarized compounds are physically explained through the orbital hybridization theory. Finally, we give a brief discussion and perspective on how to apply the PTR model on other stoichiometric materials (ABC₂ perovskites) and physical applications, such as the topology, thermoelectricity, and superconductor. Our explainable deep-learning model, systematic statistical analysis, and physical interpretation show some of the nature of flat bands, and may prompt further explorations of intrinsic flat bands in crystals and their fruitful physical, material, and device applications.

ACKNOWLEDGMENTS

The authors thank Z. Wang, J. He, J. You, and T. Yang for their helpful discussion on the DFT calculations. This work was supported by MOE, Singapore Ministry of Education

(No. A-0001160-00-00 and No. A-0005241-01-00), conducted at the National University of Singapore. The authors gratefully acknowledge the Centre of Advanced 2D Materials,

National University of Singapore and the National Supercomputing Centre of Singapore for providing computational resources.

-
- [1] J. Bardeen, L. N. Cooper, and J. R. Schrieffer, Theory of superconductivity, *Phys. Rev.* **108**, 1175 (1957).
- [2] J. Winterlik, G. H. Fecher, and C. Felser, Electronic and structural properties of palladium-based Heusler superconductors, *Solid State Commun.* **145**, 475 (2008).
- [3] Y. Cao, V. Fatemi, A. Demir, S. Fang, S. L. Tomarken, J. Y. Luo, J. D. Sanchez-Yamagishi, K. Watanabe, T. Taniguchi, E. Kaxiras *et al.*, Correlated insulator behaviour at half-filling in magic-angle graphene superlattices, *Nature (London)* **556**, 80 (2018).
- [4] M. Kang, L. Ye, S. Fang, J. S. You, A. Levitan, M. Han, J. I. Facio, C. Jozwiak, A. Bostwick, E. Rotenberg *et al.*, Dirac fermions and flat bands in the ideal kagome metal FeSn, *Nat. Mater.* **19**, 163 (2020).
- [5] G. Sethi, M. Cuma, and F. Liu, Excitonic Condensate in Flat Valence and Conduction Bands of Opposite Chirality, *Phys. Rev. Lett.* **130**, 186401 (2023).
- [6] E. Suárez Morell, J. D. Correa, P. Vargas, M. Pacheco, and Z. Barticevic, Flat bands in slightly twisted bilayer graphene: Tight-binding calculations, *Phys. Rev. B* **82**, 121407 (2010).
- [7] G. Trambly de Laissardière, D. Mayou, and L. Magaud, Numerical studies of confined states in rotated bilayers of graphene, *Phys. Rev. B* **86**, 125413 (2012).
- [8] J. M. B. Lopes dos Santos, N. M. R. Peres, and A. H. Castro Neto, Continuum model of the twisted graphene bilayer, *Phys. Rev. B* **86**, 155449 (2012).
- [9] S. Fang and E. Kaxiras, Electronic structure theory of weakly interacting bilayers, *Phys. Rev. B* **93**, 235153 (2016).
- [10] E. Tang, J. W. Mei, and X. G. Wen, High-temperature Fractional Quantum Hall States, *Phys. Rev. Lett.* **106**, 236802 (2011).
- [11] M. Kang, S. Fang, L. Ye, H. C. Po, J. Denlinger, C. Jozwiak, A. Bostwick, E. Rotenberg, E. Kaxiras, J. G. Checkelsky *et al.*, Topological flat bands in frustrated kagome lattice CoSn, *Nat. Commun.* **11**, 4004 (2020).
- [12] H. Liu, S. Meng, and F. Liu, Screening two-dimensional materials with topological flat bands, *Phys. Rev. Mater.* **5**, 084203 (2021).
- [13] T. Yang, Y. Z. Luo, Z. Wang, T. Zhu, H. Pan, S. Wang, S. P. Lau, Y. P. Feng, and M. Yang, Ag₂S monolayer: An ultrasoft inorganic Lieb lattice, *Nanoscale* **13**, 14008 (2021).
- [14] R. Shen, L. B. Shao, B. Wang, and D. Y. Xing, Single Dirac cone with a flat band touching on line-centered-square optical lattices, *Phys. Rev. B* **81**, 041410(R) (2010).
- [15] E. H. Lieb, Two Theorems on the Hubbard Model, *Phys. Rev. Lett.* **62**, 1201 (1989).
- [16] Y. Hwang, J.-W. Rhim, and B.-J. Yang, Flat bands with band crossings enforced by symmetry representation, *Phys. Rev. B* **104**, L081104 (2021).
- [17] I. Hase, T. Yanagisawa, and K. Kawashima, Flat-band in pyrochlore oxides: A first-principles study, *Nanomaterials (Basel)* **9**, 876 (2019).
- [18] I. Hase, T. Yanagisawa, Y. Aiura, and K. Kawashima, Possibility of Flat-Band Ferromagnetism in Hole-Doped Pyrochlore Oxides Sn₂Nb₂O₇ and Sn₂Ta₂O₇, *Phys. Rev. Lett.* **120**, 196401 (2018).
- [19] T. Mizoguchi, H. Katsura, I. Maruyama, and Y. Hatsugai, Flat-band solutions in D-dimensional decorated diamond and pyrochlore lattices: Reduction to molecular problem, *Phys. Rev. B* **104**, 035155 (2021).
- [20] I. Hase, T. Yanagisawa, and K. Kawashima, Computational design of flat-band material, *Nanoscale Res. Lett.* **13**, 63 (2018).
- [21] N. Regnault, Y. Xu, M.-R. Li, D.-S. Ma, M. Jovanovic, A. Yazdani, S. S. P. Parkin, C. Felser, L. M. Schoop, N. P. Ong *et al.*, Catalogue of flat-band stoichiometric materials, *Nature (London)* **603**, 824 (2022).
- [22] D. Călugăru, A. Chew, L. Elcoro, Y. Xu, N. Regnault, Z.-D. Song, and B. A. Bernevig, General construction and topological classification of crystalline flat bands, *Nat. Phys.* **18**, 185 (2021).
- [23] X. Zhang, J. Zhou, J. Lu, and L. Shen, Interpretable learning of voltage for electrode design of multivalent metal-ion batteries, *npj Comput. Mater.* **8**, 175 (2022).
- [24] K. Choudhary, K. F. Garrity, N. J. Ghimire, N. Anand, and F. Tavazza, High-throughput search for magnetic topological materials using spin-orbit spillage, machine learning, and experiments, *Phys. Rev. B* **103**, 155131 (2021).
- [25] T. Konno, H. Kurokawa, F. Nabeshima, Y. Sakishita, R. Ogawa, I. Hosako, and A. Maeda, Deep learning model for finding new superconductors, *Phys. Rev. B* **103**, 014509 (2021).
- [26] S. Lu, Q. Zhou, Y. Guo, and J. Wang, On-the-fly interpretable machine learning for rapid discovery of two-dimensional ferromagnets with high Curie temperature, *Chem.* **8**, 769 (2022).
- [27] G. Bergerhoff, R. Hundt, R. Sievers, and I. D. Brown, The inorganic crystal structure data base, *J. Chem. Inf. Comput. Sci.* **23**, 66 (1983).
- [28] S. M. Woodley and R. Catlow, Crystal structure prediction from first principles, *Nat. Mater.* **7**, 937 (2008).
- [29] E. Gossett, C. Toher, C. Oses, O. Isayev, F. Legrain, F. Rose, E. Zurek, J. Carrete, N. Mingo, A. Tropsha *et al.*, AFLOW-ML: A RESTful API for machine-learning predictions of materials properties, *Comp. Mater. Sci.* **152**, 134 (2018).
- [30] C. E. Calderon, J. J. Plata, C. Toher, C. Oses, O. Levy, M. Fornari, A. Natan, M. J. Mehl, G. Hart, M. Buongiorno Nardelli *et al.*, The AFLOW standard for high-throughput materials science calculations, *Comput. Mater. Sci.* **108**, 233 (2015).
- [31] S. Curtarolo, W. Setyawan, G. L. W. Hart, M. Jahnatek, R. V. Chepulskii, R. H. Taylor, S. Wang, J. Xue, K. Yang, O. Levy *et al.*, AFLOW: An automatic framework for high-throughput materials discovery, *Comput. Mater. Sci.* **58**, 218 (2012).
- [32] S. Curtarolo, W. Setyawan, S. Wang, J. Xue, K. Yang, R. H. Taylor, L. J. Nelson, G. L. W. Hart, S. Sanvito, M. Buongiorno-Nardelli *et al.*, AFLOWLIB.ORG: A distributed materials properties repository from high-throughput *ab initio* calculations, *Comput. Mater. Sci.* **58**, 227 (2012).
- [33] R. H. Taylor, F. Rose, C. Toher, O. Levy, K. Yang, M. Buongiorno Nardelli, and S. Curtarolo, A RESTful API for

- exchanging materials data in the AFLOWLIB.org consortium, *Comput. Mater. Sci.* **93**, 178 (2014).
- [34] A. Jain, S. P. Ong, G. Hautier, W. Chen, W. D. Richards, S. Dacek, S. Cholia, D. Gunter, D. Skinner, G. Ceder *et al.*, Commentary: The Materials Project: A materials genome approach to accelerating materials innovation, *APL Mater.* **1**, 011002 (2013).
- [35] S. P. Ong, S. Cholia, A. Jain, M. Brafman, D. Gunter, G. Ceder, and K. A. Persson, The materials application programming interface (API): A simple, flexible and efficient API for materials data based on REpresentational state transfer (REST) principles, *Comput. Mater. Sci.* **97**, 209 (2015).
- [36] J. Zhou, L. Shen, M. D. Costa, K. A. Persson, S. P. Ong, P. Huck, Y. Lu, X. Ma, Y. Chen, H. Tang *et al.*, 2DMPedia, an open computational database of two-dimensional materials from top-down and bottom-up approaches, *Sci. Data* **6**, 86 (2019).
- [37] L. Shen, J. Zhou, T. Yang, M. Yang, and Y. P. Feng, High-throughput computational discovery and intelligent design of two-dimensional functional materials for various applications, *Acc. Mater. Res.* **3**, 572 (2022).
- [38] X. Zheng, P. Zheng, and R. Z. Zhang, Machine learning material properties from the periodic table using convolutional neural networks, *Chem. Sci.* **9**, 8426 (2018).
- [39] C. Chen and S. Ong, A universal graph deep learning interatomic potential for the periodic table, *Nat. Comput. Sci.* **2**, 718 (2022).
- [40] J. Schmidt, J. Shi, P. Borlido, L. Chen, S. Botti, and M. A. L. Marques, Predicting the thermodynamic stability of solids combining density functional theory and machine learning, *Chem. Mater.* **29**, 5090 (2017).
- [41] M. Kusaba, C. Liu, Y. Koyama, K. Terakura, and R. Yoshida, Recreation of the periodic table with an unsupervised machine learning algorithm, *Sci. Rep.* **11**, 4780 (2021).
- [42] W. Ye, C. Chen, Z. Wang, I. H. Chu, and S. P. Ong, Deep neural networks for accurate predictions of crystal stability, *Nat. Commun.* **9**, 3800 (2018).
- [43] A. Y.-T. Wang, S. K. Kauwe, R. J. Murdock, and T. D. Sparks, Compositionally restricted attention-based network for materials property predictions, *npj Comput. Mater.* **7**, 77 (2021).
- [44] D. Jha, L. Ward, A. Paul, W. K. Liao, A. Choudhary, C. Wolverton, and A. Agrawal, ElemNet: Deep learning the chemistry of materials from only elemental composition, *Sci. Rep.* **8**, 17593 (2018).
- [45] I. Galanakis, P. H. Dederichs, and N. Papanikolaou, Slater-Pauling behavior and origin of the half-metallicity of the full-Heusler alloys, *Phys. Rev. B* **66**, 174429 (2002).
- [46] H. C. Kandpal, G. H. Fecher, and C. Felser, Calculated electronic and magnetic properties of the half-metallic, transition metal based Heusler compounds, *J. Phys. D* **40**, 1507 (2007).
- [47] See Supplemental Material at <http://link.aps.org/supplemental/10.1103/PhysRevMaterials.7.064804> for the prediction accuracy of each element; statistical analysis on the flat bands; atomic orbital hybridization analysis; discussion on flat-band physical properties; best flat-band for Heusler alloys. The Supplemental Material also contains Refs. [21,52].
- [48] G. Kresse and J. Furthmüller, Efficient iterative schemes for ab initio total-energy calculations using a plane-wave basis set, *Phys. Rev. B* **54**, 11169 (1996).
- [49] G. Kresse and J. Furthmüller, Efficiency of *ab initio* total energy calculations for metals and semiconductors using a plane-wave basis set, *Comput. Mater. Sci.* **6**, 15 (1996).
- [50] P. E. Blöchl, Projector augmented-wave method, *Phys. Rev. B* **50**, 17953 (1994).
- [51] J. P. Perdew, K. Burke, and M. Ernzerhof, Generalized Gradient Approximation Made Simple, *Phys. Rev. Lett.* **77**, 3865 (1996).
- [52] H. J. Monkhorst and J. D. Pack, Special points for Brillouin-zone integrations, *Phys. Rev. B* **13**, 5188 (1976).
- [53] T. Graf, C. Felser, and S. S. P. Parkin, Simple rules for the understanding of Heusler compounds, *Prog. Solid State Chem.* **39**, 1 (2011).
- [54] C. Felser, G. H. Fecher, and B. Balke, Spintronics: A challenge for materials science and solid-state chemistry, *Angew. Chem. Int. Ed.* **46**, 668 (2007).
- [55] T. Klimczuk, C. H. Wang, K. Gofryk, F. Ronning, J. Winterlik, G. H. Fecher, J. C. Griveau, E. Colineau, C. Felser, J. D. Thompson *et al.*, Superconductivity in the Heusler family of intermetallics, *Phys. Rev. B* **85**, 174505 (2012).
- [56] J. H. Wernick, G. W. Hull, T. H. Geballe, J. E. Bernardini, and J. V. Waszczak, Superconductivity in ternary Heusler intermetallic compounds, *Mater. Lett.* **2**, 90 (1983).
- [57] I. Galanakis, P. Mavropoulos, and P. H. Dederichs, Electronic structure and Slater-Pauling behaviour in half-metallic Heusler alloys calculated from first principles, *J Phys. D* **39**, 765 (2006).
- [58] Y. Cao, V. Fatemi, S. Fang, K. Watanabe, T. Taniguchi, E. Kaxiras, and P. Jarillo-Herrero, Unconventional superconductivity in magic-angle graphene superlattices, *Nature (London)* **556**, 43 (2018).
- [59] C. S. Chiu, D.-S. Ma, Z.-D. Song, B. A. Bernevig, and A. A. Houck, Fragile topology in line-graph lattices with two, three, or four gapped flat bands, *Phys. Rev. Res.* **2**, 043414 (2020).
- [60] H. Luo, X. Li, Y. Wang, Y. Jin, M. Yao, and J. Yang, High-throughput screening of room temperature active Peltier cooling materials in Heusler compounds, *npj Comput. Mater.* **8**, 199 (2022).
- [61] M. Markov, S. E. Rezaei, S. N. Sadeghi, K. Esfarjani, and M. Zebarjadi, Thermoelectric properties of semimetals, *Phys. Rev. Mater.* **3**, 095401 (2019).
- [62] J. He, M. Amsler, Y. Xia, S. S. Naghavi, V. I. Hegde, S. Hao, S. Goedecker, V. Ozolins, and C. Wolverton, Ultralow Thermal Conductivity in Full Heusler Semiconductors, *Phys. Rev. Lett.* **117**, 046602 (2016).
- [63] D. I. Bilc, G. Hautier, D. Waroquiers, G. M. Rignanese, and P. Ghosez, Low-dimensional Transport and Large Thermoelectric Power Factors in Bulk Semiconductors by Band Engineering of Highly Directional Electronic States, *Phys. Rev. Lett.* **114**, 136601 (2015).
- [64] S. Waki, Y. Yamaguchi, and K. Mitsugi, Superconductivity of Ni₂NbX (X = Al, Ga and Sn), *J Phys. Soc. Jpn.* **54**, 1673 (1985).
- [65] <https://github.com/mpeshel/AI-for-flat-band-materials>.